

# Observations of PSR J1357–6429 at 2.1 GHz with the Australia Telescope Compact Array

A. Kirichenko,<sup>1,2\*</sup> Yu. Shibano<sup>1,2</sup> P. Shternin,<sup>1,2</sup> S. Johnston,<sup>3</sup> M. A. Voronkov,<sup>3,4,5</sup>  
A. Danilenko,<sup>1</sup> D. Barsukov,<sup>1,2</sup> D. Lai<sup>6</sup> and D. Zyuzin<sup>1</sup>

<sup>1</sup>*Ioffe Institute, 26 Politekhnicheskaya st., St. Petersburg 194021, Russia*

<sup>2</sup>*Peter the Great St. Petersburg Polytechnic University, 29 Politekhnicheskaya st., St. Petersburg 195251, Russia*

<sup>3</sup>*CSIRO Astronomy and Space Science, Australia Telescope National Facility, PO Box 76, Epping, NSW 1710, Australia*

<sup>4</sup>*Astro Space Centre, Profsovnaya st. 84/32, 117997 Moscow, Russia*

<sup>5</sup>*School of Mathematics and Physics, University of Tasmania, GPO Box 252-37, Hobart, Tasmania 7000, Australia*

<sup>6</sup>*Department of Astronomy, Cornell University, Ithaca, NY 14853, USA*

Accepted XXX. Received YYY; in original form ZZZ

## ABSTRACT

PSR J1357–6429 is a young and energetic radio pulsar detected in X-rays and  $\gamma$ -rays. It powers a compact pulsar wind nebula with a jet visible in X-rays and a large scale plerion detected in X-ray and TeV ranges. Previous multiwavelength studies suggested that the pulsar has a significant proper motion of about 180 mas yr<sup>−1</sup> implying an extremely high transverse velocity of about 2000 km s<sup>−1</sup>. In order to verify that, we performed radio-interferometric observations of PSR J1357–6429 with the the Australia Telescope Compact Array (ATCA) in the 2.1 GHz band. We detected the pulsar with a mean flux density of  $212 \pm 5 \mu\text{Jy}$  and obtained the most accurate pulsar position, RA = 13:57:02.525(14) and Dec = −64:29:29.89(15). Using the new and archival ATCA data, we did not find any proper motion and estimated its 90 per cent upper limit  $\mu < 106 \text{ mas yr}^{-1}$ . The pulsar shows a highly polarised single pulse, as it was earlier observed at 1.4 GHz. Spectral analysis revealed a shallow spectral index  $\alpha_\nu = 0.5 \pm 0.1$ . Based on our new radio position of the pulsar, we disclaim its optical counterpart candidate reported before.

**Key words:** Pulsars: individual: PSR J1357–6429

## 1 INTRODUCTION

Born in supernova explosions, neutron stars (NSs) typically obtain velocities orders of magnitude greater than those of their stellar progenitors. According to statistical analyses (see [Hobbs et al. 2005](#)), the mean three-dimensional velocities of NSs mostly derived from radio data are about 400 km s<sup>−1</sup>. The largest firmly established pulsar transverse velocity of  $1080 \pm 100 \text{ km s}^{-1}$ , which has been determined by direct proper motion and parallax measurements with the VLBA, belongs to PSR B1508+55 ([Chatterjee et al. 2005](#)).

Although an initial kick which occurs during supernova explosions is generally accepted as the reason for high velocities, the origin of the kick is currently unclear. [Lai et al. \(2001\)](#) discuss several classes of kick mechanisms, but it is not clear whether any of them can fully explain the fastest moving neutron stars (e.g., [Chatterjee et al. 2005](#)). Therefore, new detections of high-velocity pulsars are needed to

put additional constraints on models used in the latest supernova explosion simulations (see [Wongwathanarat et al. 2013](#)). The velocity measurements might be also potentially useful to reveal possible relationship between the velocity and other parameters of NSs ([Lai et al. 2001](#)).

PSR J1357–6429 is a young (characteristic age 7.3 kyr) and energetic (spin-down luminosity  $\dot{E} = 3.1 \times 10^{36} \text{ ergs s}^{-1}$ ) radio pulsar with a period of 166 ms ([Camilo et al. 2004](#)). The pulse profile and polarisation were studied with the Parkes telescope at 1.4 GHz by [Camilo et al. \(2004\)](#); [Johnston & Weisberg \(2006\)](#); [Lemoine-Goumard et al. \(2011\)](#) and [Rookyard et al. \(2015\)](#). The pulsar field was observed in X-rays, where the pulsar counterpart and a compact tail-like pulsar wind nebula (PWN), implying a noticeable pulsar proper motion, were found ([Esposito et al. 2007](#); [Zavlin 2007](#)). Thorough follow-up high-energy studies have revealed X-ray and  $\gamma$ -ray pulsations with the pulsar period ([Lemoine-Goumard et al. 2011](#); [Chang et al. 2012](#)). A pulsar plerion extended to a few tens of arcminutes was detected in X-ray and TeV ranges

\* E-mail: aida.astro@mail.ioffe.ru (AK)

by Abramowski et al. (2011). They also argued that the extended radio emission from the supernova remnant (SNR) candidate G309.8–2.6 (Duncan et al. 1997) is rather the pleion counterpart.

Danilenko et al. (2012) reported the detection of a faint pulsar optical counterpart candidate with the Very Large Telescope (VLT) whose position was in an agreement with PSR J1357–6429 X-ray position. However, a significant offset ( $1''.54 \pm 0''.32$ ) of the candidate position from the J1357–6429 radio-interferometric coordinates measured 8.7 yr earlier by Camilo et al. (2004) with the Australia Telescope Compact Array (ATCA), rises some doubts about the pulsar nature of the candidate and/or suggests that the pulsar has an extremely high proper motion.

The distance to the pulsar of  $\sim 2.5$  kpc was estimated from its dispersion measure  $DM = 128.5 \text{ pc cm}^{-3}$  by Camilo et al. (2004). Danilenko et al. (2012) performed an independent distance analysis comparing the interstellar extinction–distance relation along the pulsar line of sight and the absorbing column density obtained from the X-ray spectral analysis. The resulting distance range of 2.0–2.5 kpc supports the DM distance estimate. The distance range and the candidate offset imply the pulsar transverse velocity to be between  $1300 \text{ km s}^{-1}$  and  $2500 \text{ km s}^{-1}$ , which is higher than the largest NS velocity precisely measured so far (Chatterjee et al. 2005). A similar velocity range was estimated from the comparison of the pulsar X-ray and radio-interferometric positions (Mignani et al. 2011).

Aiming to check whether the pulsar velocity is indeed that high, we performed new radio-interferometric observations with the ATCA to obtain a precise pulsar position for another epoch. Another reason for the observations was to extend the radio studies of the pulsar itself, which was investigated only at 1.4 GHz, to a higher frequency range. The details of observations and data reduction are described in Sect. 2. Our results and reanalysis of the archival data are presented in Sect. 3 and summarised in Sect. 4.

## 2 OBSERVATIONS AND DATA REDUCTION

The observations of the pulsar field were carried out with the ATCA on 2013 June 3. The observing session started at UT 4:30 and lasted for 9.5 hours. The main goal of the observations was to measure a precise position of the source. Therefore, the observations were performed with the 6C array configuration, which has the maximum baseline of nearly 6 km. We used the pulsar binning capability of the Compact Array Broadband Backend (CABB), which allowed us to perform high time resolution observations (Wilson et al. 2011). The binning mode split the 166 ms pulsar period into 32 independent rotational phase bins. The observations were carried out in the 16 cm band centred at 2.102 GHz. The total bandwidth of 2.048 GHz was split into 512 spectral channels providing 4 MHz spectral resolution in the 1.078–3.126 GHz range. PKS B1934–638 was observed at the beginning of the session as a primary standard for the flux density scale and bandpass calibrations. To account for gain and phase instabilities, we observed two nearby secondary calibrators 1329–665 and 1325–55 in a ten-minute loop with the pulsar, where each calibrator was observed for about two minutes. Two calibrators were used to estimate

the systematic errors on the position reference frame. Standard data reduction including Radio Frequency Interference (RFI) flagging and calibration was performed with MIRIAD package (Sault et al. 1995), and Karma (Gooch 1996) tools were used for data visualisation.

The data were split into four 512 MHz sub-bands with central frequencies of 1.334 GHz, 1.846 GHz, 2.358 GHz and 2.870 GHz. The secondary calibration was then performed separately for each bandwidth partition.

The data were imaged using the MIRIAD *invert* task with the “robust” parameter set to zero. It provides a trade-off between better signal-to-noise ratio ( $S/N$ ) and stronger sidelobe suppression in the visibility weighting scheme. The deconvolution process was performed with the *mfclean* routine, which accounts for spectral variations across the bandwidth. For the purposes of absolute astrometry, we used the resulting clean images without further calibration.

Phase self-calibration was performed on the data to improve the image quality. After the first iteration of *mfclean*, model components with flux densities  $\gtrsim 1 \text{ mJy beam}^{-1}$  were used for the initial multi-frequency phase self-calibration, which considerably decreased residual phase errors. Then the weaker sources found on clean images were included in the self-calibration model. As a result, after several clean-self-calibration cycles, the sidelobes of field sources became comparable with the thermal noise of  $\approx 50 \text{ } \mu\text{Jy beam}^{-1}$  for the 1.334 GHz subband and  $\approx 25\text{--}30 \text{ } \mu\text{Jy beam}^{-1}$  for the three other sub-bands.

For the lower (1.334 GHz) and higher (2.870 GHz) frequency sub-bands, the synthesised beam size was  $8''.3 \times 5''.1$  and  $4''.5 \times 2''.6$ , respectively, with the position angle  $PA \approx -24^\circ$ . The ATCA primary beam full width at half maximum (FWHM) was  $42'$  for the lowest frequency, decreasing to  $15'$  for the highest frequency. The selected image size for all sub-bands was  $\sim 160' \times 160'$ .

To confidently measure the pulsar proper motion, we performed an independent analysis of the available archival ATCA data<sup>1</sup>. The set was obtained on 2000 August 29 in the 6A configuration with the baselines close to those of 6C but in 1.376 and 2.496 GHz bands with 128 MHz bandwidths each split in 14 spectral channels (Camilo et al. 2004)<sup>2</sup>. The data processing and imaging were similar to those applied to our own set, except that no splitting was performed and the gain calibration was done with the single observed calibrator 1329–665. The synthesised beam size was  $12''.7 \times 5''.6$  with  $PA \approx 48^\circ$  and  $7''.3 \times 2''.2$  with  $PA \approx 40^\circ$  for 1.376 and 2.496 GHz, respectively. The imaging procedure for the 1.376 GHz band revealed a point-like source surrounded by concentric sidelobe-like rings which were difficult to clean off. The source is located close to the phase centre and the pulsar, and was not identified in the 2013 images. Thorough data inspection showed that it only appears in channels 13 and 14 near the low frequency sideband and thus is likely spurious. Given its proximity to the pulsar, we used only channels 1–12 to eliminate the artifact and its sidelobes which could affect the pulsar position and flux measurements.

<sup>1</sup> <http://atoa.atnf.csiro.au>, project CX001.

<sup>2</sup> The 2.496 GHz data were not reported by Camilo et al. (2004).

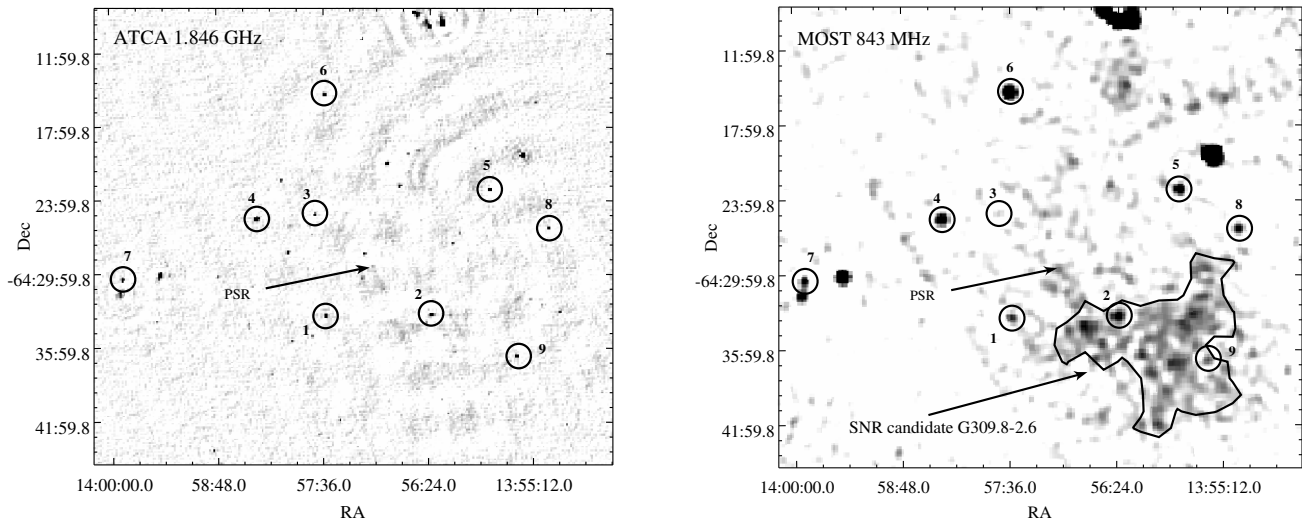


**Figure 1.**  $50' \times 50'$  field fragment centred at the PSR J1357–6429 as it is visible with the ATCA (*left*) and the MOST (*right*) at 1.846 GHz and 843 MHz, respectively. The positions of the pulsar and the extended emission from the SNR candidate G309.8–2.6 surrounded by the contour are indicated by arrows. Numbered circles mark nine bright point-like objects used for the relative astrometry of the ATCA images (see text for details).

### 3 RESULTS

#### 3.1 The pulsar field

In Fig. 1, we show the self-calibrated image of the pulsar field in the 1.846 GHz sub-band. For comparison, we also present the Molonglo Observatory Synthesis Telescope (MOST) image at 843 MHz with a restoring beam size of  $\approx 104''$  (Murphy et al. 2007). Many MOST point-like objects have their firm counterparts in the ATCA image and vice versa. The pulsar is detected with the ATCA as a point-like source at a  $10\sigma$  significance in this sub-band and is also visible in the MOST image.

Due to significantly higher spatial resolution of the ATCA, several MOST sources are resolved as groups of separate objects. For instance, a bright extended object near the north edge of the MOST image is actually a blend of three compact objects. At the same time, insufficient uv-coverage and the long baseline configuration make the interferometer insensitive to large extended structures. That is why the extended emission from the SNR candidate G309.8–2.6 (Duncan et al. 1997) and other extended structures visible in the MOST image cannot be identified in the ATCA image.

The compact NE-SW tail-like PWN structure of J1357–6429 visible in X-rays (Chang et al. 2012) is not seen in the radio.

#### 3.2 The astrometry and pulsar proper motion

To constrain the pulsar proper motion, we used two astrometric methods. The first one, which we hereafter refer to as “absolute astrometry”, allows to measure source coordinates relative to phase calibrators, whose positions are known with a high accuracy, for instance, from the VLBI measurements. The second approach, which we entitle “relative astrome-

try”, is based on measurements of the target position shift between observational epochs relative to other sources in the field.

In all cases, to measure the pulsar positions, we used on-pulse data obtained from the calibrated visibilities. Using the *MIRIAD* *psrfix* routine, the pulse-phase bins were phase-adjusted as a function of frequency channel accounting for the known DM of  $128.5 \text{ pc cm}^{-3}$  and the pulsar period of 166 ms. After that, a mean off-pulse baseline value was subtracted with the *psrbl* tool. This considerably decreased the pulsar contamination by backgrounds.

##### 3.2.1 Absolute astrometry

We obtained eight positions of the pulsar in the 2013 images, for each of the four spectral sub-bands in both secondary calibrations. They were determined with the *MIRIAD* task *imfit* using the object type “point”. The position uncertainty derived with this task slightly depends on the size of a region around the pulsar where the fit is performed. We used a region of about twice the synthesised beam size in each sub-band. We checked that the resulting positional errors were comparable to the size of the beam, divided by twice the (S/N). The S/N was  $\approx 11.2$ , 9.1, 10.8 and 6.4 for the 1.334, 1.846, 2.358 and 2.780 GHz sub-bands, respectively. To provide better position measurements, the pixel grid on the on-pulse images was adjusted to place the pulsar exactly in the pixel centre. The positions measured in each sub-band were found to be consistent within uncertainties, indicating that no correction for systematic errors between the sub-bands is needed (Deller et al. 2009).

The mean pulsar positions for 1325–665 and 1329–55 calibrations weighted over the four sub-bands are  $\text{RA} = 13:57:02.526(15)$ ,  $\text{Dec} = -64:29:29.95(15)$  and  $\text{RA} =$

13:57:02.524(14), Dec =  $-64:29:29.85(12)^3$ , respectively. The best-fit positions and the positional error ellipses are shown in Fig. 2 with crosses and inner thin solid and dashed ellipses for 1325–65 and 1329–55 calibrations, respectively. The positional error ellipse projected on the  $1\sigma$  coordinate uncertainty represents only 40 per cent 2D confidence region (e.g., Press et al. 2002). For completeness, we also show 90 per cent confidence ellipses, which are by a factor  $\approx 2.14$  larger in size. The two measured positions show  $\approx 0''.12$  systematic offset in Dec. We checked that it is consistent with the shift obtained after cross-calibrating the 1325–665 and 1329–55 standards and measuring their positions. According to Fig. 2, the estimated systematic error along the synthesized beam major principle axis is comparable with the formal statistical  $1\sigma$  uncertainty. Therefore, the two source positions were weighted by the respective covariance matrices, in order to account for correlations between the errors in RA and Dec, and combined. The resulting mean position with 40 per cent and 90 per cent uncertainties are shown in Fig. 2 with the bold cross and ellipses. The uncertainties were obtained by adding the estimated systematic covariance matrix to the weighted mean statistical covariance matrix. The final coordinates are RA = 13:57:02.525(14) and Dec =  $-64:29:29.89(15)$ , where  $1\sigma$  errors correspond to the inner bold ellipse in Fig. 2.

The derived position appears to be different from RA = 13:57:02.43(2) and Dec =  $-64:29:30.2(1)$  provided by Camilo et al. (2004) based on the 2000 ATCA 1.376 GHz observations implying that the pulsar has moved between 2000 and 2013 epochs.

To check the pulsar shift significance, we remeasured the pulsar position on the 1.376 GHz on-pulse image of the 2000 data where the pulsar is detected with  $S/N \approx 13$ . At 2.496 GHz, the pulsar is found at a significantly lower  $S/N$ , making the position measurements less accurate. The derived 1.376 GHz coordinates are RA = 13:57:02.546(76) and Dec =  $-64:29:29.64(55)^4$ . They are consistent with the ones stated by Camilo et al. (2004). However, the published uncertainties appeared to be considerably smaller than the estimate based on the synthesised beam size and the pulsar  $S/N$ . We thereby conclude that the published pulsar position errors were severely underestimated.

In Fig. 3, we show the pulsar full-band on-pulse images obtained for two epochs using the same calibrator (1329–665). The pulsar positions for the two observational epochs with the respective error ellipses at 40 and 90 per cent confidence levels, which account for the systematics mentioned above, are overlaid on the images. No significant pulsar shift is visible and only an upper limit of  $\approx 1''.28$  (90 per cent) can be established. Accounting for that and a time-base of 12.76 yr between the two ATCA observations, the 90 per cent upper limit on the pulsar proper motion is  $\mu \lesssim 100 \text{ mas yr}^{-1}$ .

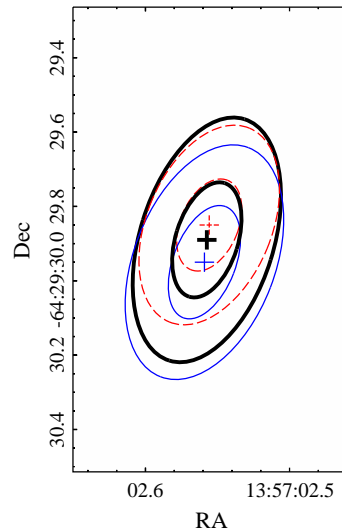


**Figure 2.** Pulsar position uncertainty ellipses measured at 40 and 90 per cent confidence levels in 2.1 GHz band. Thin solid and dashed line crosses and ellipses correspond to the calibrations obtained with 1329–665 and 1325–55 standards, respectively. The bold cross and solid bold line ellipses are the derived weighted mean positions.

### 3.2.2 Relative astrometry

Relative astrometry is generally considered as a more robust tool which allows to account for systematic effects which cannot be excluded in advance. For instance, comparing 2000 and 2013 positions of various sources in the field, we found that they exhibit systematic shifts between the epochs, directed roughly radially from the phase centre and increasing with the offset from it. This stretch could result from bandwidth smearing which was slightly different for pre-CABB and CABB data. There also can be a small rotation between epochs caused by different ephemeris codes used for pre-CABB and CABB correlators.

To increase the image dynamic range and reduce the positional errors, we used the self-calibrated images for each of the 2013 sub-bands, as well as for the 2000 epoch. The pulsar  $S/N$  was slightly increased as compared to the non-self-calibrated case and was  $\approx 18, 9.9, 11.8$  and  $8.1$  for the 1.334, 1.846, 2.358 and 2.780 GHz sub-bands, respectively, while in the 2000 image the  $S/N$  remained the same. Self-calibration, however, introduced some shift due to an incomplete sky model. The five images were aligned using a custom-built routine which accounts for shifts, rotations and stretches. For referencing, we used nine relatively bright point-like sources detected in all images with the signal-to-noise ratio  $\gtrsim 30$ . They are shown in Fig. 1 and their positions were determined using *imfit* routine with an accuracy  $\lesssim 0''.07$ . We found the stretch by a factor of 1.0021(3) and a small rotation by 1.2(6) arcmin for the 2000 image with

<sup>3</sup> Herein, the numbers in brackets are  $1\sigma$  uncertainties referring to the last significant digits quoted, the equinox is J2000.0.

<sup>4</sup> The systematics cannot be accounted here since only one secondary calibrator was observed.



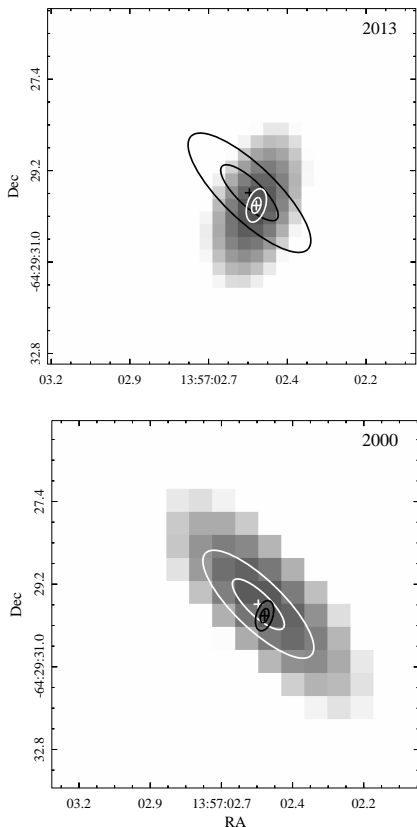


**Figure 3.**  $8'' \times 8''$  ATCA image fragments with PSR J1357–6429 in the centre obtained from the non-self-calibrated data at 2.102 GHz in 2013 (*top*) and at 1.376 GHz in 2000 (*bottom*) epochs using the same calibrator and with pixel scales of  $0''.25$  and  $0''.5$ , respectively. For a given epoch the derived pulsar position and the 40 and 90 per cent position uncertainties are shown by the white cross and ellipses, while the black cross and ellipses are related to the other epoch. The images were used for absolute astrometry.

respect to the 2013 images. Neither significant stretch nor rotation between different sub-bands of 2013 observations were found. After the transformation, positions of the reference sources in all images became consistent within the uncertainties. The pulsar proper motion was included in the routine and was fitted simultaneously with the reference solution.

In Fig. 4, the mean of the pulsar positions in the aligned 2013 sub-bands is compared with the 2000 position. We find that the arrangement of the pulsar error ellipses on epochs 2000 and 2013 slightly differs from that provided by the absolute astrometry (cf., Fig. 3), while again no significant shift between the epochs is seen. The 40, 90 and 99.73 per cent confidence regions on the pulsar proper motion  $\mu_\alpha \cos \delta_0$  and  $\mu_\delta$  are shown in Fig. 5. The 90 per cent upper limit on the pulsar proper motion, which is the radius of the circular region containing 90 per cent probability, is  $\mu < 106 \text{ mas yr}^{-1}$ . This value is compatible, but slightly higher than the result obtained from the absolute astrometry. The reason for this is that the positional errors of the 2000 data are in fact underestimated in the absolute astrometry method

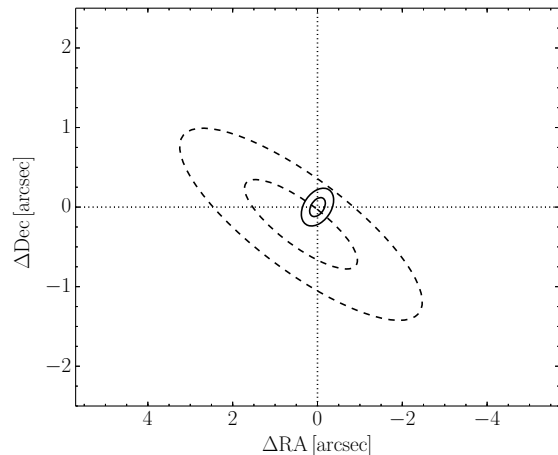


**Figure 4.** 40 and 90 per cent pulsar position uncertainty ellipses after relative astrometry. The 2013 and 2000 positions are shown by solid and dashed ellipses, respectively. The positions are shown relative to the mean pulsar position at the 2013 epoch. The offsets differ from those presented in Fig. 3 for the absolute astrometry.

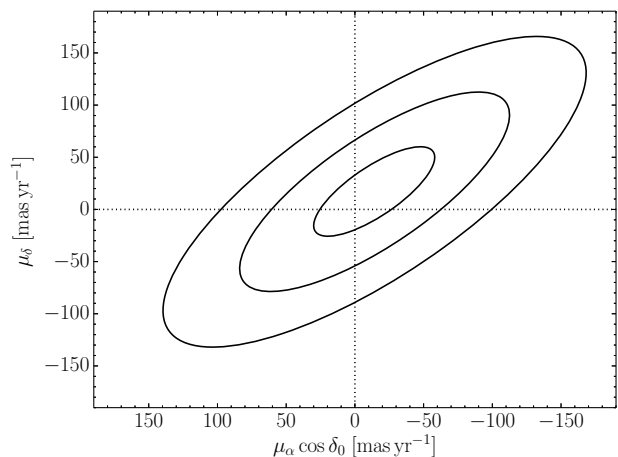


**Figure 5.** 40, 90 and 99.73 per cent confidence regions of the pulsar proper motion based on the relative astrometry.  $\cos \delta_0 \approx 0.43$ , where  $\delta_0$  is the declination of the phase centre for the 2013 epoch data.

since the systematic errors are not accessible. Therefore, we believe that the relative astrometry results are more reliable.

### 3.3 The pulsar flux densities and spectrum

To measure the pulsar flux, we used self-calibrated on-pulse visibilities. To study the spectrum in detail, we additionally split each 512 MHz sub-band in half. In order to exclude possible errors introduced by the non-linear cleaning algorithms, we measured the flux directly from the visibility data using the MIRIAD *uvfit* routine. The pulsar position, however, was fixed at the values obtained with the *imfit* on the corresponding clean images. The measured fluxes are shown in Fig. 6 by solid error-bar crosses. The mean flux over the full 2013 band is  $212 \pm 5 \mu\text{Jy}$ . The spectral energy distribution

shows a noticeable flux depression at  $\approx 1.7$  GHz. The resulting spectrum excluding this point can be fitted by a single power-law with a spectral index  $\alpha_\nu = 0.5 \pm 0.1$  (reduced  $\chi^2 \approx 0.8$ ). The depression significance in respect of the fit is  $\approx 3\sigma$ . The inclusion of this point makes the fit unacceptable (reduced  $\chi^2 \approx 2.3$ ). The depression can hardly be explained by any interstellar absorption at the pulsar line of sight, e.g. owing to OH 1.665 and 1.667 GHz lines. There are only 3 pulsars, where weak OH absorption features with FWHM of 1.5–3 km s<sup>-1</sup> are observed (e.g., Minter 2005, and references therein). Such features cannot lead to the observed flux depression in our case. In addition, we inspected background objects and found a similar feature at 1.7 GHz in spectra of the sources located within  $\approx 2.5$  of the phase centre, while the sources located at larger angular distances and the calibrators do not show this feature. Based on this we suppose that the feature is a systematic artifact and exclude it from the pulsar spectral fit<sup>5</sup>.

The pulsar fluxes on the 2000 data were measured using the full-band self-calibrated 1.376 GHz and 2.496 GHz visibilities. The respective fluxes of  $417 \pm 58 \mu\text{Jy}$  and  $309 \pm 86 \mu\text{Jy}$  are shown in Fig. 6 by dashed error-bar crosses. Given the large uncertainties of the 2000 observations, it is difficult to make any conclusion about the spectral index. However, the 2000 flux values appear to be larger than those of the 2013 data, at least for the lower frequency. The pulsar flux at 1.376 GHz in the 2000 data differs from that in 2013 by about  $2.5\sigma$  including 2 per cent flux calibration uncertainties<sup>6</sup>. The difference significance is thus about 99 per cent.

It is possible that the flux variability can be attributed to the long-term refractive scintillation (e.g., Lorimer & Kramer 2012). Using the galactic electron density model NE2001 of Cordes & Lazio (2002) we estimated the field coherence scale  $s_0 \approx 4900$  km, the Fresnel scale  $l_F \approx 1.6 \times 10^6$  km and the refractive scale  $l_R = l_F^2/s_0 \approx 5.2 \times 10^8$  km at 1.376 GHz for the pulsar line of sight. Given that  $l_F \ll l_R$ , the intensity modulation index due to the refractive scintillation can be estimated as  $m_R = (s_0/l_R)^{1/6} \approx 0.15$  (Lorimer & Kramer 2012). This value is consistent with the observed 1.376 GHz flux modulation between the two epochs  $(F_{2000} - F_{2013})/(F_{2000} + F_{2013}) = 0.16 \pm 0.08$ . For the Kolmogorov turbulence spectrum, the modulation index scales with the frequency as  $m_R \propto \nu^{0.56}$  and at 2.496 GHz is larger by a factor of 1.4 than at 1.376 GHz. This is not excluded by the data. The timescale of the flux variability due to the refractive scintillation  $\Delta t_R = l_R/v_{tr}$  is inversely proportional to the pulsar transverse velocity  $v_{tr}$ . Using the derived upper limit on the pulsar proper motion we estimated the lower limit  $\Delta t_R \gtrsim 6$  days, which is significantly larger than the duration of our observations.

### 3.4 The pulse profile and polarisation

We studied the pulse and polarisation profiles of the 2013 epoch in the same eight 256 MHz sub-bands. The phase-resolved  $I$ ,  $Q$ ,  $U$  and  $V$  Stokes parameters were extracted

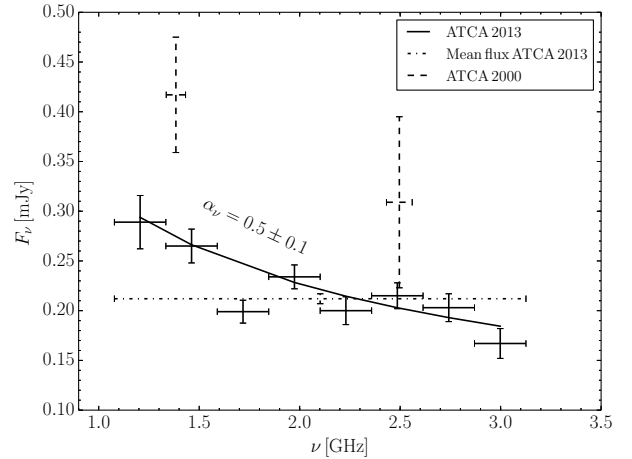


**Figure 6.** ATCA spectrum of PSR J1357–6429. Solid vertical error-bars are the flux densities with  $1\sigma$  uncertainties in sub-bands shown by horizontal solid bars with 256 MHz widths regularly spaced within the whole 1.1–3.1 GHz band. The line represents the best fit of the measured fluxes by the power law  $F_\nu \propto \nu^{-\alpha_\nu}$  with a spectral index  $\alpha_\nu$  shown in the plot. Mean flux densities in the whole 2.102 GHz band measured without division by sub-bands and in 1.376 and 2.496 GHz bands of 2000 are shown by dot-dashed and dashed error-bars for comparison. The systematic flux calibration uncertainties of  $\lesssim 2$  per cent are negligible in this scale.

using the *MIRIAD* *psrplt* routine. The pulsar emission is observable in five adjacent phase bins. We found no significant profile width and polarisation changes across the whole 2.102 GHz band. As an example, the resulting pulse profiles for the Stokes  $I$ , the circular polarisation  $V$  and the linearly polarised component  $L = (Q^2 + U^2)^{1/2}$  in the 2.358 GHz sub-band are shown in the lower right panel of Fig. 7. The intensity profile shows a relatively wide single component. The pulse FWHM of  $32^\circ \pm 3^\circ$  obtained using a Gaussian profile fit, virtually 100 per cent of the linear polarisation and small amount of circular polarisation are fully consistent with the higher time and spectral resolution 1.4 GHz data obtained with the Parkes telescope (Johnston & Weisberg 2006; Rookyard et al. 2015). For completeness, in the lower-left panel in Fig. 7 we show the same profiles for the 1.376 GHz band of the 2000 data set. These data demonstrate somewhat wider intensity profile with FWHM  $\approx 43^\circ \pm 4^\circ$ . The broader pulse profile observed in the 2000 data can partially result from the DM smearing of  $\approx 9^\circ$  due to a twice as low spectral resolution with the channel width of  $\approx 9$  MHz. The smearing in the 2013 data at the same frequency is less significant,  $\approx 4^\circ$ , and it does not affect the pulse profiles at higher frequencies. Accounting for the DM smearing and the profile fit uncertainties, the 2000 and 2013 intrinsic pulse widths appear to be consistent.

The large bandwidth of the 2013 data allowed us to infer the rotation measure (RM) along the pulsar line of sight utilising the  $\lambda^2$  dependence of the linear polarisation position angle  $\psi$ . The latter values and their errors were determined from the Stokes parameters  $Q$  and  $U$  measured in the five on-pulse phase bins with the *uvfit* routine (as described in Sec. 3.3) for each of the eight spectral sub-bands.

<sup>5</sup> According to the operation team, the flux depression can be caused by a correlator issue in the pulsar binning mode.

<sup>6</sup> See, e.g., <http://www.narrabri.atnf.csiro.au/observing/users/guide/html/chunked/ch02s02.html>

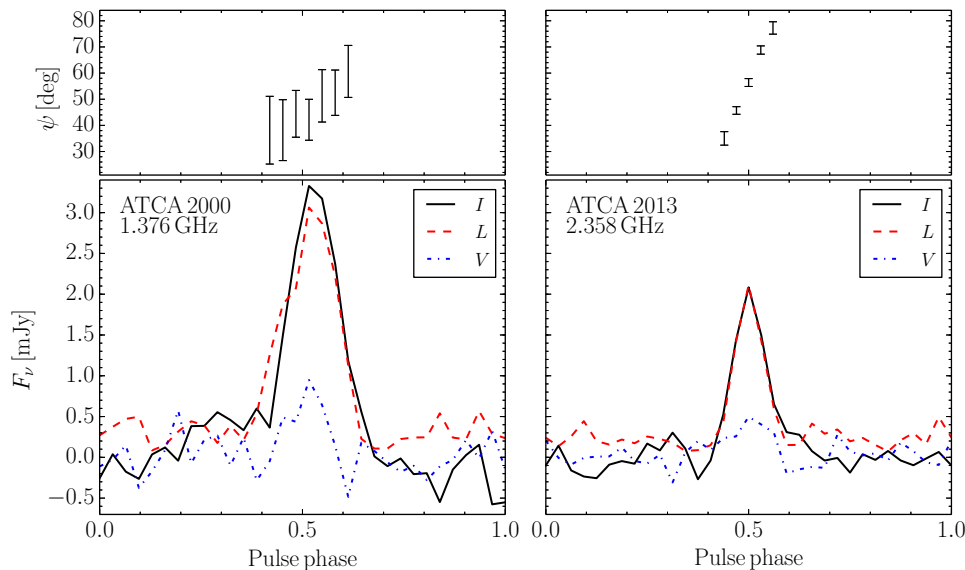


**Figure 7.** Pulse and polarisation profiles (*bottom*), and linear polarisation angle  $\psi$  (*top*) for PSR J1357–6429 obtained with the ATCA at 1.376 GHz (*left*) and 2.358 GHz (*right*). One full period is shown. Solid, dashed and dot-dashed lines show the total intensity  $I$ , linearly polarised component  $L = (Q^2 + U^2)^{1/2}$  and circular polarisation  $V$ , respectively.  $\psi$  is corrected for RM and shown for on-pulse phases. Phase of 0.5 is placed at the flux density peak.

The linear fit to the observed  $\psi(\lambda^2)$  dependence was performed in each phase bin in order to check for the possible RM variation with phase (Noutsos et al. 2009). The resulting RM values were found to be consistent within uncertainties, therefore the global fit for  $\psi(\lambda^2)$  dependence was performed with RM value tied between all five bins. The initial regression was not good, with  $\chi^2 = 1.79$  for 34 degrees of freedom, indicating that either position angle errors were underestimated or there exists a non-trivial spectral behaviour of the position angle. Indeed, the data for two lowest frequency bands in our set likely show a shallower swing of  $\psi$  than in the other six sub-bands. Since the reason for such behaviour is unclear, we conservatively increased the errors of the measured  $\psi$  values to make  $\chi^2$  of the global fit equal one. The resulting RM of  $-43 \pm 1 \text{ rad m}^{-2}$  is smaller, but consistent with  $-47 \pm 2 \text{ rad m}^{-2}$  estimated from the Parkes Telescope 1.4 GHz data obtained with a narrow bandwidth (Johnston & Weisberg 2006). We note also, that the RM fit for the six upper frequencies is successful without any error renormalisation, however giving smaller RM of  $-37 \pm 1 \text{ rad m}^{-2}$ . Therefore, we can not exclude the spectral variations of the RM, as observed for some pulsars (Dai et al. 2015). The illustration of the  $\psi(\lambda^2)$  dependence for the central phase bin is shown in Fig. 8. The solid line with grey-hatched region in Fig. 8 show the best-fit linear regression with 68 per cent uncertainty region.

The phase-dependence of the position angle in the five on-pulse bins, corrected for the rotation measure, is shown in the top-right panel in Fig. 7. This dependence is clearly linear with the slope  $C = 0.96 \pm 0.03$ . As expected, the results for 1.376 GHz data of 2000 observations are consistent with the 2013 measurements (Fig. 7, top-left panel). They are also consistent with the higher time resolution data obtained with the Parkes telescope (Rookyard et al. 2015). The  $\psi$ -phase dependence demonstrates almost no curvature.

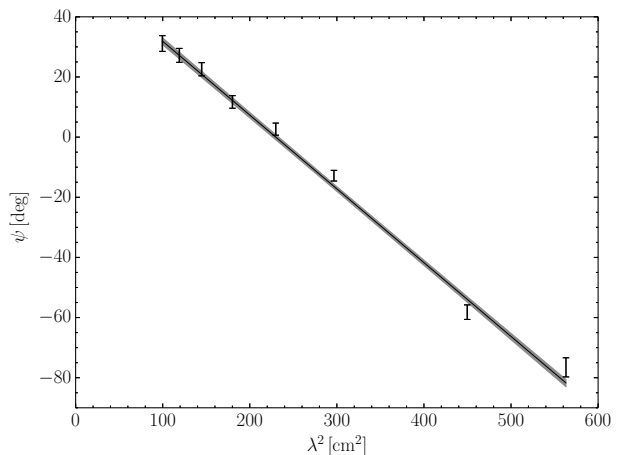


**Figure 8.** Polarization angle  $\psi$  against the square of the observing wavelength  $\lambda$ . The grey-hatched region shows 68 per cent linear fit uncertainty.

Therefore, virtually any pulsar emission geometry can be fitted to the data, according to the classical rotation vector model (RVM; Radhakrishnan & Cooke 1969). Using a more detailed  $\psi$  curve, Rookyard et al. (2015) obtained loose constraints on the angle between the magnetic and the rotation axes  $\alpha$ . However, the authors favoured the almost aligned rotator with  $\alpha \approx 7^\circ$ .

While RVM does not provide robust constraints on the pulsar emission geometry from our data, it is nevertheless possible to invoke additional arguments basing on the observed pulse profile width and the statistical data on other pulsars. Gil et al. (1984) showed that the half-opening angle of the pulsar beam  $\rho_q$  (at a certain relative intensity level  $q$ )

can be related to the pulse width  $W_q$  at the same level via the expression

$$\cos \rho_q = \cos \alpha \cos(\alpha + \beta) + \sin \alpha \sin(\alpha + \beta) \cos(W_q/2), \quad (1)$$

where  $\beta$  is the angle of the closest impact of the line of sight to the magnetic axis. In addition, the slope of the positional angle curve at the inflection point is related to the angles  $\alpha$  and  $\beta$  via the relation

$$\sin \alpha = C \sin \beta \quad (2)$$

(Komesaroff 1970). Utilising these equations and the value for the pulse FWHM of  $W_{50} = 32^\circ$ , we can find the angles  $\alpha$ ,  $\beta$  and  $\rho_{50}$  for any line of sight position  $\zeta = \alpha + \beta$ . The resulting solution varies in the broad range, however the ratio  $|\beta|/\rho_{50}$ , i.e. the value of the impact parameter in units of the emission cone radius, is tied in the narrow range of 0.93–1 for all  $\zeta$ . Similar solutions with  $W_{10} = 70^\circ$  give  $|\beta|/\rho_{10} \in (0.77, 1)$ . This suggests that the line of sight passes at the edge of the beam with the rotation of the star. One can try to extract the real value of  $\rho$  from the statistical data on other pulsars. The diagram of the pulse widths  $vs$  period has a clear low boundary which, in case of the core component, is thought to represent the value of  $\rho$  for orthogonal rotators ( $\alpha \approx \pi/2$ ) with low impact parameters ( $\beta \approx 0$ ) (Rankin 1990; Maciesiak & Gil 2011). In this case, the main source of the difference of the observed width from the minimal value is described by

$$W_{\text{obs}} = \frac{W_{\text{min}}}{\sin \alpha} \quad (3)$$

(Rankin 1990; Maciesiak & Gil 2011). Using the low boundary from Maciesiak & Gil (2011), we can estimate the inclination angle  $\alpha$  to be about  $10^\circ$  on the basis of the  $W$  measurements alone. Note, that according to Maciesiak & Gil (2011), this method can overestimate  $\alpha$  in the close-to-aligned cases (low  $\alpha$ ). However, it is more likely that the single pulse of PSR J1357–6429 is the cut of the cone component at its side because of the observed high linear and low circular polarisations (Lyne & Manchester 1988). Maciesiak et al. (2012) argue that the estimate (3) is still applicable for the conal profiles, provided impact angle  $\beta$  is small. It is not likely in the case of PSR J1357–6429. Since the relative contributions of the profile broadening with  $\alpha$  and narrowing with  $\beta$  are not known in advance, we employed the method suggested by Malov & Nikitina (2011). The authors recommend to use the mean value of the observed pulse widths  $W$  in the sample of pulsars with similar periods as the conservative estimate for twice the value of  $\rho$ . The expression (9) from Malov & Nikitina (2011) yields  $\rho_{10} \approx 13^\circ$  for the PSR J1357–6429 period. From the Eqs. (1) and (2) we again obtained  $\alpha \approx 10^\circ$ , in accordance with the simple estimate from Eq. (3) and the favoured solution of Rookyard et al. (2015).

#### 4 SUMMARY

The new ATCA observations of the PSR J1357–6429 allowed us to detect the pulsar in the 1.1–3.1 GHz band, to measure its accurate position, the intensity and polarisation pulse profiles, to derive the RM in a wide frequency range and to study the pulsar spectrum. Comparing our results

with the archival ATCA 2000 data at 1.376 and 2.496 GHz, we examined variation of the pulsar flux, pulse profile and polarisation, and constrained the pulsar proper motion.

Based on the ATCA 2013 data, the pulsar has a single pulse component with a constant pulse width of about  $32^\circ$  over the whole 1.078–3.126 GHz frequency range. The radiation has a high, almost 100 per cent, linear polarisation, which is typical for young pulsars with  $\dot{E} \gtrsim 10^{34}$  erg s $^{-1}$  (Weltevrede & Johnston 2008). We do not detect spectral variation of the linear polarisation degree. The pulse profile shape and polarisation properties are in agreement with the Parkes telescope 1.4 GHz observations (Camilo et al. 2004; Johnston & Weisberg 2006; Lemoine-Goumard et al. 2011; Rookyard et al. 2015) and the ATCA 1.376 GHz observations in 2000. An apparent increase of the observed pulse width in the 2000 data set is mainly due to the DM smearing caused by the worse spectral resolution. The pulsar spectral energy distribution extracted from the 2013 data demonstrates a shallow spectral index of about 0.5. The ATCA 2000 flux values appear to be larger than those of the 2013 data, at least for the lower frequency. This variability can result from the effects of the refractive interstellar scintillation on the timescales significantly larger than the duration of our observations. Detailed monitoring campaign is necessary to check this (e.g., Bhat et al. 1999).

The rotation measure estimate of  $-43 \pm 1$  rad m $^{-2}$  is compatible within  $2\sigma$  with the previous narrow band measurements but appears to be more reliable since it is obtained using a wider frequency range. Based on the derived RM, we estimated the mean Galactic magnetic field along the pulsar line of sight  $\bar{B} = 1.23 \times 10^{-6}$  RM/DM =  $-0.41 \pm 0.01$   $\mu$ G. This is close to the values for most of other pulsars from the ATNF catalogue<sup>7</sup> located within a  $2^\circ$  circle around the pulsar position.

On the basis of the absolute and relative astrometry methods, we did not detect the proper motion of the pulsar. We estimated a 90 per cent upper limit on it of about 100 mas yr $^{-1}$  which corresponds to the pulsar transverse velocity  $v_{tr} \lesssim 1200$  km s $^{-1}$  if the DM distance of 2.5 kpc is adopted. This does not contradict the value of  $\sim 650$  km s $^{-1}$  suggested by Abramowski et al. (2011) based on the offset of the pulsar from the centre of the extended source HESS J1356–645, possibly associated with the pulsar plerion. The reason of the discrepancy with the extremely high pulsar transverse velocity suggested by Mignani et al. (2011) and Danilenko et al. (2012) is a strong underestimation of the uncertainties of the pulsar radio coordinates derived from the ATCA 2000 observations by Camilo et al. (2004). Our analysis shows that further radio observations with at least the same spatial resolution as provided by the ATCA 2013 data, will allow one to constrain the pulsar proper motion shift with accuracy  $\lesssim 0''.15$ .

The new ATCA position of the pulsar can be compared with the position of the suggested candidate to the pulsar optical counterpart (Danilenko et al. 2012). The ATCA 68 per cent error ellipse is overlaid on the VLT  $I$ -band image adapted from Danilenko et al. (2012) and shown in Fig. 9. The pulsar X-ray positions obtained with *Chandra* are also

<sup>7</sup> <http://www.atnf.csiro.au/research/pulsar/psrcat/>, Manchester et al. (2005)



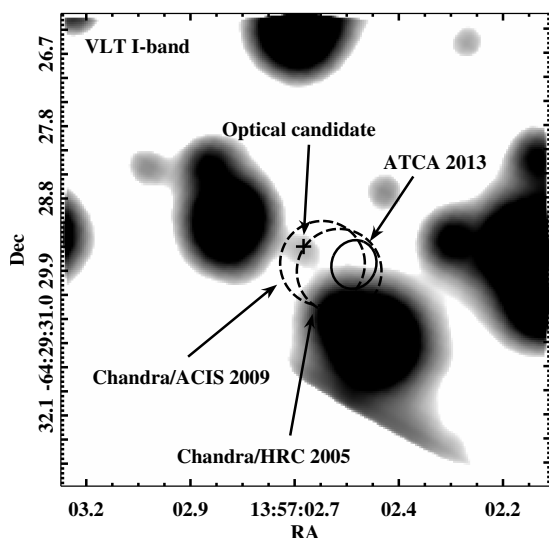


**Figure 9.** Fragment of the pulsar field imaged with VLT/FORS2 in *I*-band (Danilenko et al. 2012). The pulsar optical counterpart candidate position is shown by the cross. *Chandra* and ATCA pulsar positions are shown by  $1\sigma$  error ellipses. These ellipses also account for the optical astrometric referencing uncertainty of  $0''.2$ .

presented. Given a higher accuracy of the ATCA pulsar position as compared with the X-ray positions, we conclude that the optical candidate can be discarded as the pulsar counterpart at a 99 per cent significance. A relatively bright star is located in  $\sim 1''$  southwards the new radio position of the pulsar, and further searching for its faint optical counterpart is only possible with a high spatial resolution imaging provided either by the HST or ground-based optical telescopes with adaptive optics systems.

## ACKNOWLEDGEMENTS

We are grateful to the referee Adam Deller for his comments which prompted us to reconsider certain parts of the manuscript. Authors thank E. B. Nikitina, I. F. Malov, F. Camilo, Serge Balashev and D. E. Alvarez-Castillo for useful discussions. The work was supported by the Russian Science Foundation, grant 14-12-00316. The Australia Telescope Compact Array is part of the Australia Telescope National Facility which is funded by the Commonwealth of Australia for operation as a National Facility managed by CSIRO.

## REFERENCES

- Abramowski A., et al., 2011, *A&A*, **533**, A103  
 Bhat N. D. R., Rao A. P., Gupta Y., 1999, *ApJS*, **121**, 483  
 Camilo F., et al., 2004, *ApJL*, **611**, L25  
 Chang C., Pavlov G. G., Kargaltsev O., Shibano Y. A., 2012, *ApJ*, **744**, 81  
 Chatterjee S., et al., 2005, *ApJL*, **630**, L61  
 Cordes J. M., Lazio T. J. W., 2002, *ArXiv Astrophysics e-prints*,  
 Dai S., et al., 2015, *MNRAS*, **449**, 3223

- Danilenko A., Kirichenko A., Mennickent R. E., Pavlov G., Shibano Y., Zharikov S., Zyuzin D., 2012, *A&A*, **540**, A28  
 Deller A. T., Tingay S. J., Briske W., 2009, *ApJ*, **690**, 198  
 Duncan A. R., Stewart R. T., Haynes R. F., Jones K. L., 1997, *MNRAS*, **287**, 722  
 Esposito P., Tiengo A., de Luca A., Mattana F., 2007, *A&A*, **467**, L45  
 Gil J., Gronkowski P., Rudnicki W., 1984, *A&A*, **132**, 312  
 Gooch R., 1996, in Jacoby G. H., Barnes J., eds, *Astronomical Society of the Pacific Conference Series Vol. 101, Astronomical Data Analysis Software and Systems V*. p. 80  
 Hobbs G., Lorimer D. R., Lyne A. G., Kramer M., 2005, *MNRAS*, **360**, 974  
 Johnston S., Weisberg J. M., 2006, *MNRAS*, **368**, 1856  
 Komesaroff M. M., 1970, *Nature*, **225**, 612  
 Lai D., Chernoff D. F., Cordes J. M., 2001, *ApJ*, **549**, 1111  
 Lemoine-Goumard M., et al., 2011, *A&A*, **533**, A102  
 Lorimer D. R., Kramer M., 2012, *Handbook of Pulsar Astronomy*  
 Lyne A. G., Manchester R. N., 1988, *MNRAS*, **234**, 477  
 Maciesiak K., Gil J., 2011, *MNRAS*, **417**, 1444  
 Maciesiak K., Gil J., Melikidze G., 2012, *MNRAS*, **424**, 1762  
 Malov I. F., Nikitina E. B., 2011, *Astronomy Reports*, **55**, 878  
 Manchester R. N., Hobbs G. B., Teoh A., Hobbs M., 2005, *AJ*, **129**, 1993  
 Mignani R. P., Shearer A., de Luca A., Moran P., Collins S., Marelli M., 2011, *A&A*, **533**, A101  
 Minter A. H., 2005, in *American Astronomical Society Meeting Abstracts*. p. 1301  
 Murphy T., Mauch T., Green A., Hunstead R. W., Piestrzynska B., Kels A. P., Sztajer P., 2007, *MNRAS*, **382**, 382  
 Noutsos A., Karastergiou A., Kramer M., Johnston S., Stappers B. W., 2009, *MNRAS*, **396**, 1559  
 Press W. H., Teukolsky S. A., Vetterling W. T., Flannery B. P., 2002, *Numerical recipes in C++ : the art of scientific computing*  
 Radhakrishnan V., Cooke D. J., 1969, *ApL*, **3**, 225  
 Rankin J. M., 1990, *ApJ*, **352**, 247  
 Rookyard S. C., Weltevred P., Johnston S., 2015, *MNRAS*, **446**, 3367  
 Sault R. J., Teuben P. J., Wright M. C. H., 1995, in Shaw R. A., Payne H. E., Hayes J. J. E., eds, *Astronomical Society of the Pacific Conference Series Vol. 77, Astronomical Data Analysis Software and Systems IV*. p. 433 ([arXiv:astro-ph/0612759](https://arxiv.org/abs/astro-ph/0612759))  
 Weltevred P., Johnston S., 2008, *MNRAS*, **391**, 1210  
 Wilson W. E., et al., 2011, *MNRAS*, **416**, 832  
 Wongwathanarat A., Janka H.-T., Müller E., 2013, *A&A*, **552**, A126  
 Zavlin V. E., 2007, *ApJL*, **665**, L143

This paper has been typeset from a  $\text{\LaTeX}$  file prepared by the author.